

Electron charge qubit with 0.1 millisecond coherence time

Xianjing Zhou,^{1,2,*} Xinhao Li,^{1,*} Qianfan Chen,¹ Gerwin Koolstra,³ Ge Yang,^{4,5} Brennan Dizdar,⁶ Yizhong Huang,² Christopher S. Wang,⁶ Xu Han,^{1,2} Xufeng Zhang,⁷ David I. Schuster,^{2,6,8,†} and Dafei Jin^{1,2,9,‡}

¹Center for Nanoscale Materials, Argonne National Laboratory, Lemont, Illinois 60439, USA

²Pritzker School of Molecular Engineering, University of Chicago, Chicago, Illinois 60637, USA

³Computational Research Division, Lawrence Berkeley National Laboratory, Berkeley, California 94720, USA

⁴The NSF AI Institute for Artificial Intelligence and Fundamental Interactions, USA

⁵Computer Science and Artificial Intelligence Laboratory, Massachusetts Institute of Technology, Cambridge, Massachusetts 02139, USA

⁶James Franck Institute and Department of Physics, University of Chicago, Chicago, Illinois 60637, USA

⁷Department of Electrical and Computer Engineering, Northeastern University, Boston, Massachusetts 02115, USA

⁸Department of Applied Physics, Stanford University, Stanford, California 94305, USA

⁹Department of Physics and Astronomy, University of Notre Dame, Notre Dame, Indiana 46556, USA

(Dated: 21 February 2023)

Electron charge qubits are compelling candidates for solid-state quantum computing because of their inherent simplicity in qubit design, fabrication, control, and readout. However, all existing electron charge qubits, built upon conventional semiconductors and superconductors, suffer from severe charge noise that limits the coherence time to the order of 1 microsecond. Here, we report our experimental realization of ultralong-coherence electron charge qubits, based upon isolated single electrons trapped on an ultraclean solid neon surface in vacuum. Quantum information is encoded in the motional states of an electron that is strongly coupled with microwave photons in an on-chip superconducting resonator. The measured relaxation time T_1 and coherence time T_2 are both on the order of 0.1 milliseconds. The single-shot readout fidelity without using a quantum-limited amplifier is 98.1%. The average single-qubit gate fidelity using Clifford-based randomized benchmarking is 99.97%. Simultaneous strong coupling of two qubits with the same resonator is demonstrated, as a first step toward two-qubit entangling gates for universal quantum computing. These results manifest that the electron-on-solid-neon (eNe) charge qubits outperform all existing charge qubits to date and rival state-of-the-art superconducting transmon qubits, offering an appealing platform for quantum computing.

Quantum bits (qubits) are the fundamental building blocks in quantum information processing. A key measure of a qubit's performance is its coherence time, which describes how long a superposition between two quantum states $|0\rangle$ and $|1\rangle$ can persist¹. Among a handful of on-chip solid-state qubits today^{2,3}, a coherence time on the order of 0.1 ms or longer has only been achieved in semiconductor quantum-dot and donor qubits based on electron spins⁴⁻⁷, and superconducting transmon and fluxonium qubits based on capacitively and inductively shunted Josephson junctions⁸⁻¹¹. By contrast, the coherence time in the traditional semiconductor quantum-dot qubits and superconducting Cooper-pair-box (CPB) qubits based on electron charges (motional states) is at most on the order of $1\ \mu\text{s}$ ^{4,12}. Given that a typical gate time is around 10 ns in such systems, in order to make electron charge qubits serious contenders for quantum computing, it is imperative to increase their coherence time to at least the order of 0.1 ms, that is, a $\gtrsim 10^4$ ratio between the coherence and gate times¹³.

The short coherence time for conventional electron charge qubits is commonly recognized as a result of their high sensitivity to environmental noise, *e.g.*, charge fluctuations in ordinary host materials^{7,14}. Nonetheless, if their coherence time can be substantially prolonged, electron charge qubits will possess unique advantages: (i) They can be conveniently designed and fabricated with no need of spin-purified substrates⁶ or

patterned micromagnets¹⁵, significantly reducing the manufacturing cost¹⁶. (ii) They can be fully electrically controlled with no involvement of magnetic fields¹⁷, intrinsically eliminating the compatibility issues between magnetic fields and superconducting circuits^{18,19}. (iii) They can be individually addressed and readout by microwave photons owing to the much stronger coupling between an electric dipole and electric field than a magnetic dipole and magnetic field^{4,20}, fundamentally avoiding the complexities of high microwave power²¹ or spin-charge conversion^{15,22}.

In this paper, we report our experimental realization of unconventional electron charge qubits with 0.1 ms long coherence time, based upon single electrons trapped on a solid neon surface²³. Neon (Ne), as a noble-gas element, is inert against forming chemical bonds with any other elements. In a low-temperature and near-vacuum environment, it spontaneously condenses into an ultrapure semi-quantum solid²⁴ devoid of any two-level-system (TLS) fluctuators, quasiparticles, or dangling bonds that are present in most ordinary materials^{17,25}. Its small atomic polarizability and negligible spinful isotopes make it akin to vacuum with minimal charge and spin noise for electron qubits^{24,26}. By integrating an electron trap in a superconducting quantum circuit, the charge (motional) states of an electron can be controlled and readout by microwave photons in an on-chip resonator. Our previous demonstration of the electron-on-solid-neon (eNe) qubit platform has shown

an appreciable relaxation time T_1 of 15 μs and coherence time T_2 of 220 ns²³.

Here we successfully extend both T_1 and T_2 into 0.1 ms time scale by making three critical advancements: (i) annealing solid Ne to pursue the best surface quality, (ii) stabilizing the electron trapping potential to ensure the lowest (< 10 Hz) background noise, and (iii) operating the qubit at charge-noise-insensitive (sweet) spots. With 0.1 ms long coherence time, we manage to perform single-shot readout of the qubit states²⁷ and obtain a 98.1% readout fidelity without using a quantum-limited amplifier. This is on par with the readout fidelity of the state-of-the-art transmon qubits with a similar amplification chain^{27,28}. We further manage to perform Clifford-based randomized benchmarking²⁹ and obtain an average single-qubit gate fidelity of 99.97%, which is well above the fault-tolerance threshold for quantum error correction with surface codes³⁰. Moreover, we manage to simultaneously couple two electron qubits with the same resonator, as a first step toward two-qubit entangling gates for universal quantum computing³¹. These results manifest that the eNe charge qubits outperform all traditional semiconductor and superconducting charge qubits and rival the best superconducting transmon qubits today.

Qubit design

The eNe qubit is situated in an electron trap in a niobium (Nb) superconducting quantum circuit that is fabricated on an intrinsic silicon (Si) substrate, as shown in Fig. 1a. A channel of 3.5 μm in width and 1 μm in depth is etched into the substrate. A quarter-wavelength double-stripline microwave resonator runs on the bottom through the channel. A dc electrode, called the trap, also runs on the bottom, but from the other end of the channel into the open end of the resonator. The channel, resonator, and trap are all deformed into oval shapes in the trapping region to accommodate the desired functionalities as described below. On the ground plane outside the channel, four additional dc electrodes, made into two pairs and called the resonator-guards and trap-guards respectively, surround the trapping region. The dc bias voltages applied to these dc electrodes, as well as the resonator with a tuning-fork structure³², tune the trapping potential. We ensure the lowest charge noise from our apparatus by using an ultra-stable high-precision digital-to-analog converter (DAC) at room temperature and lowpass filters with 10 Hz cutoff frequency at mK temperature.

The qubit states $|0\rangle$ and $|1\rangle$ are defined by the electron's motional (charge) states, *i.e.*, the ground state $|g\rangle$ and the first excited state $|e\rangle$ respectively, in the y -direction across the channel. The electric dipole transition between $|g\rangle$ and $|e\rangle$ strongly couples with the electric field, which points from one stripline to the other, of the microwave photons in the antisymmetric (differential) mode of the resonator^{23,32}. The bare resonator frequency, defined after neon filling but before electron-photon coupling, is $\omega_r/2\pi = f_r = 6.4262$ GHz.

The resonator linewidth is $\kappa/2\pi = 0.46$ MHz, which is dominated by the input and output photon coupling. All the microwave measurements are done in a transmission configuration through the resonator.

We fill a controlled amount of liquid Ne into the sample cell, using a homemade gas-handling puff system, to wet the channel and quantum circuit at around 26 K. We cool the system down along the liquid-vapor coexistence line and turn the liquid into solid by passing the solid-liquid-gas triple point at the temperature $T_t = 24.6$ K and pressure $P_t = 0.43$ bar³³. We hold the temperature at 10 K for 1–2 hours to anneal the solid and smooth out the surface³⁴, and then continuously cool down to the base temperature around 10 mK for experiments. The thickness of solid Ne that covers the trapping region is estimated to be tens of nanometers. Electrons are emitted from a heated tungsten filament above the quantum circuit and are trapped on the solid Ne surface under the combined actions of natural surface potential and applied electric potential^{23,24,35,36}.

Qubit spectroscopy

We first verify the strong coupling between a trapped single electron and microwave photons in the circuit quantum electrodynamics (cQED) architecture (see Methods). By varying the resonator-guard voltage V_{rg} and keeping all other voltages fixed, we tune the qubit frequency f_q across f_r . The normalized transmission amplitude $(A/A_0)^2$ through the resonator is plotted in Fig. 1b. Two avoided crossings, known as the vacuum Rabi splitting, can be clearly seen. A line cut in Fig. 1b at the on-resonance condition $f_q = f_r$, marked by the pink arrows, is plotted in Fig. 1c. By fitting the curve with the input-output theory, we obtain the electron-photon (qubit-resonator) coupling strength $g/2\pi = 2.3$ MHz, and the on-resonance qubit linewidth $\gamma/2\pi = 0.36$ MHz. The fact that $g > \kappa > \gamma$ indicates that the qubit and resonator are strongly coupled. In this vacuum Rabi splitting measurement, the average intra-resonator photon number \bar{n} is kept below 1, as can be verified by the ac Stark effect³⁷ (see Methods).

We use two-tone qubit spectroscopy to reveal the qubit spectrum tuned by V_{rg} , as plotted in Fig. 1d. The dependence of f_q on V_{rg} can be identified as the white curve, where the drive frequency f_d hits f_q and induces a sudden phase shift. The spectrum suggests that f_q is nearly a quadratic function of V_{rg} and contains a minimum at the so-called charge sweet spot, as indicated by the yellow arrow. On this spot, where $f_q = f_{\text{ss}} = 6.3915$ GHz and $V_{\text{rg}} = V_{\text{ss}} = -270$ mV, the charge qubit is first-order insensitive to the low-frequency charge noise and holds the longest coherence time along the spectrum³⁸.

State control and readout

We perform real-time state control and readout on the eNe qubit in the dispersive regime. Rabi oscillations³⁹ are observed by driving the qubit on the sweet spot, using Gaussian-shaped microwave pulses with fixed frequency f_q and amplitude A_{pulse} , and variable pulse duration

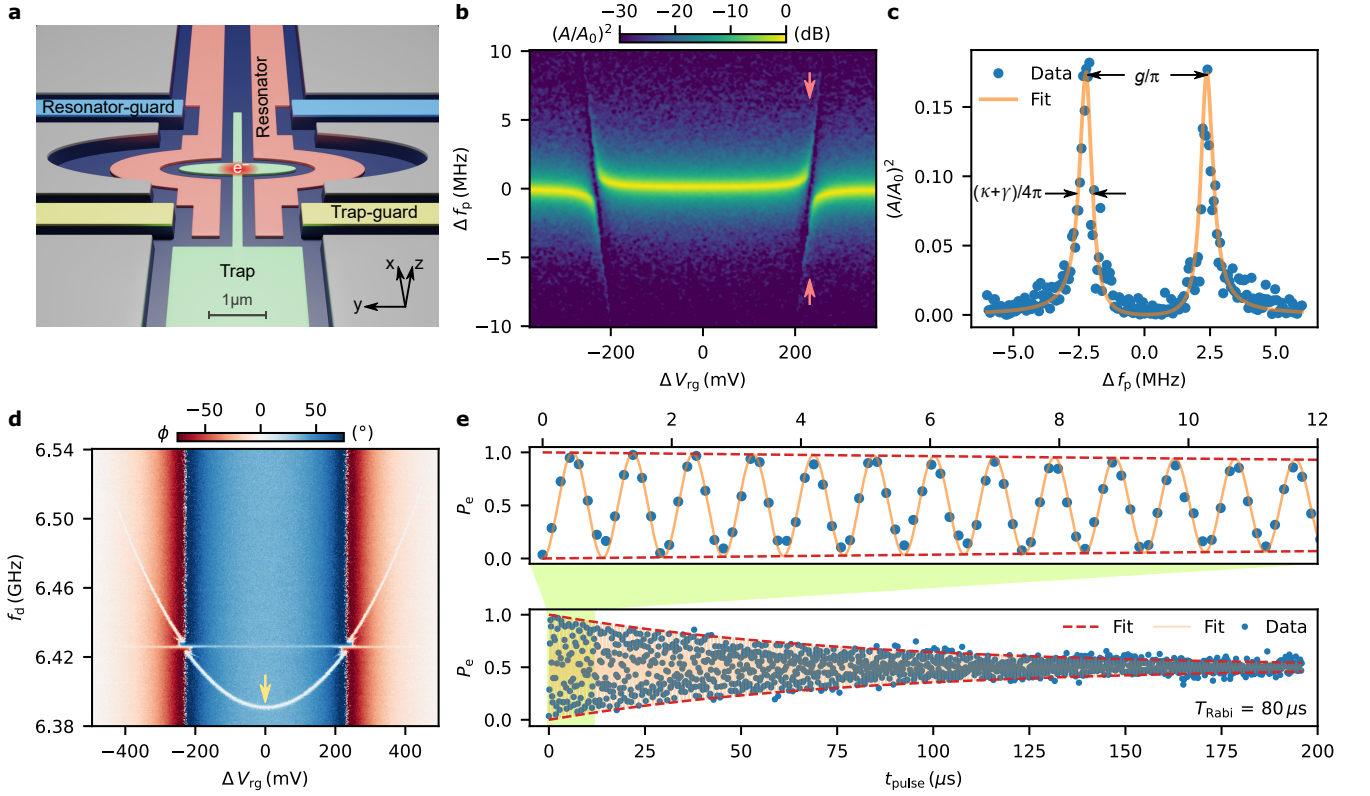


Fig. 1 | Design and properties of an electron-on-solid-neon (eNe) charge qubit. **a**, Schematic of the device. A single electron is trapped on a solid Ne surface in the oval region of the channel. Its qubit spectrum is tuned by the dc electrodes around and its motional states in y are coupled with the electric field of microwave photons in the double-stripline resonator. **b**, Observation of vacuum Rabi splitting. The normalized microwave transmission amplitude $(A/A_0)^2$ through the resonator is plotted versus the offset probe frequency $\Delta f_p = f_p - f_r$ and the offset resonator-guard voltage $\Delta V_{rg} = V_{rg} - V_{ss}$, where V_{ss} is the value of V_{rg} on the sweet spot pointed by the yellow arrow in **d**. The pink arrows mark the on-resonance condition when $f_q = f_r$. **c**, Line plot of $(A/A_0)^2$ versus Δf_p at the value of V_{rg} indicated by the pink arrows in **b**, where the qubit and resonator are on resonance, $f_q = f_r$. The two peaks give the coupling strength g and the qubit linewidth γ when $f_q = f_r$. **d**, Two-tone measurement of qubit spectrum. The microwave transmission phase ϕ through the resonator is measured at the probe-tone frequency f_p (fixed at the bare resonator frequency $f_p = f_r$) and is plotted against a simultaneously applied drive-tone frequency f_d and ΔV_{rg} . The white curve shows the nearly quadratic dependence of qubit frequency f_q on ΔV_{rg} . The yellow arrow indicates the minimum called the charge sweet spot. **e**, Observation of Rabi oscillations in short and long time scales. The excited-state population P_e is plotted versus the microwave pulse duration t_{pulse} with a fixed amplitude and qubit frequency. The orange solid curve fits the exponentially decaying sinusoidal oscillations and the red dashed curve fits the exponentially decaying envelop. The fitted Rabi decay time is $T_{\text{Rabi}} = 80 \mu\text{s}$.

t_{pulse} . The oscillations of qubit states detected by dispersive readout²⁰ (see Methods) are plotted in two (short and long) time scales in Fig. 1e. The Rabi decay time $T_{\text{Rabi}} = 80 \mu\text{s}$ is obtained by an exponential fit to the envelope of oscillatory population P_e in the excited state in the large time scale. Such a long T_{Rabi} indicates both a long relaxation time T_1 and a long pure-dephasing time T_φ , the latter of which is related to the total coherence time T_2 via $T_2^{-1} = (2T_1)^{-1} + T_\varphi^{-1}$. Theoretically, in the absence of inhomogeneous broadening and under a strong driving electric field, T_{Rabi} is related to T_1 and T_φ by $1/T_{\text{Rabi}} = 3/(4T_1) + 1/(2T_\varphi)$ ^{40,41}.

Relaxation and coherence times

We then find the characteristic times of the eNe qubit, *i.e.*, the relaxation time T_1 , the total dephasing (Ramsey)

time T_2^* , and the total coherence time with a Hahn echo T_{2E} . These characteristic times provide key measures of single-qubit performance.

The total relaxation (decay) rate $T_1^{-1} = \Gamma = \Gamma_R + \Gamma_{\text{NR}}$ is the sum of radiative decay rate $\Gamma_R = \kappa g^2 / \Delta^2$, which is determined by the Purcell effect^{42,43}, and nonradiative decay rate Γ_{NR} . On the sweet spot, the measured T_1 is $48.2 \mu\text{s}$, as shown in the upper panel of Fig. 2a. With the known values of g , κ , and $\Delta/2\pi = -34.7 \text{ MHz}$ on the sweet spot, we find a radiative decay time $\Gamma_R^{-1} = 78.7 \mu\text{s}$ and nonradiative decay time $\Gamma_{\text{NR}}^{-1} = 125 \mu\text{s}$. This suggests that the Purcell-limited radiative decay is the dominant decay channel here. We verify this by purposely moving away from the sweet spot to a point with a larger detuning, $\Delta/2\pi = 100 \text{ MHz}$. It gives an

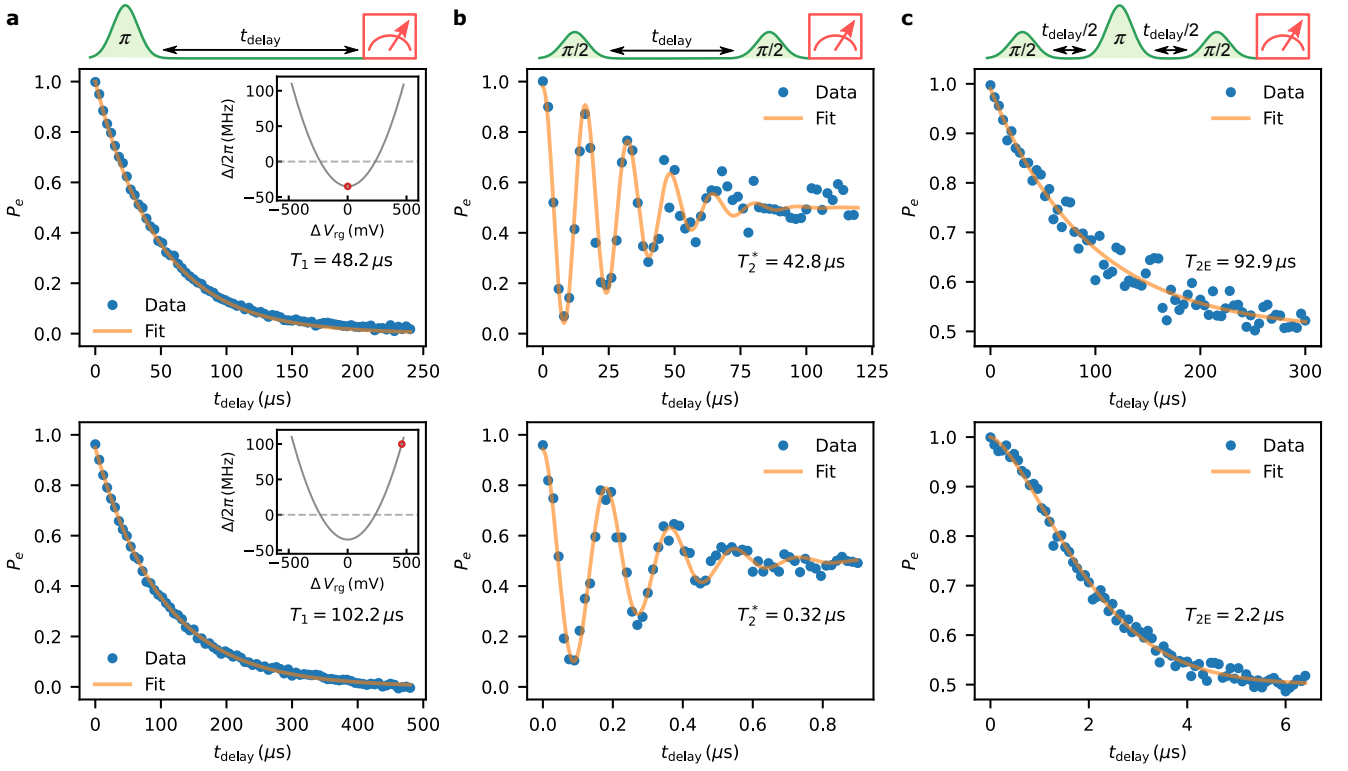


Fig. 2 | Time-domain characterization of an electron-on-solid-neon (eNe) charge qubit. **a**, Relaxation time measurements of the qubit on (upper panel) and off (lower panel) the sweet spot. The sweet spot is at the minimum of the qubit spectrum detuned by $\Delta/2\pi = -34.7$ MHz from the bare resonator frequency and the non-sweet spot is chosen at a point with large slope on the qubit spectrum detuned by $\Delta/2\pi = 100$ MHz, as indicated by the circles in the insets. The excited-state population P_e is plotted versus the delay time t_{delay} between the readout pulse and the π -gate pulse. The fitted relaxation time is $T_1 = 48.2 \mu\text{s}$ and $102.2 \mu\text{s}$, on and off the sweet spot respectively. **b**, Ramsey-fringe measurements of the qubit on and off the sweet spot. P_e is plotted versus the delay time t_{delay} between two $\pi/2$ -gate pulses. The fitted total dephasing time is $T_2^* = 42.8 \mu\text{s}$ and $0.32 \mu\text{s}$, on and off the sweet spot respectively. **c**, Hahn-echo measurements of the qubit on and off the sweet spot. P_e is plotted versus the delay time t_{delay} between two $\pi/2$ -gate pulses separated by a π -gate pulse in the middle. The fitted total coherence time (with a Hahn echo) is $T_{2E} = 92.9 \mu\text{s}$ and $2.2 \mu\text{s}$, on and off the sweet spot respectively.

even longer T_1 of $102.2 \mu\text{s}$, as shown in the lower panel of Fig. 2a, which agrees with the sum of the estimated Γ_R at this detuning and the Γ_{NR} above.

On the sweet spot, the first-order insensitivity of the qubit frequency to the low-frequency charge noise yields exceedingly long total dephasing time T_2^* and total coherence time with a Hahn echo T_{2E} . Our Ramsey-fringe measurement gives a $T_2^* = 42.8 \mu\text{s}$, as shown in the upper panel of Fig. 2b. To our knowledge, this is the longest observed charge-qubit dephasing time, compared with all existing semiconductor quantum-dot and superconducting CPB charge qubits^{2,3,11,44}. The low-frequency noise can be further suppressed by applying echo pulses. Our Hahn-echo measurement gives a $T_{2E} = 92.9 \mu\text{s}$ that almost equals $2T_1$, as shown in the upper panel of Fig. 2c. This means that, on the sweet spot, the residual decoherence that cannot be mitigated by Hahn echoes is dominated by relaxation. As a comparison, we purposely move off the sweet spot to a point more sensitive to charge noise at 100 MHz detuning. The observed T_2^* decreases to $0.32 \mu\text{s}$ and T_{2E} decreases

to $2.2 \mu\text{s}$, as shown in the lower panels of Fig. 2b and 2c.

For the completeness of our investigation, we slightly change the Ne thickness and make another eNe qubit that has a larger detuning on the sweet spot, $\Delta/2\pi = -288$ MHz, which more strongly suppresses the Purcell-limited radiative decay. This qubit shows a much longer $T_1 = 82.8 \mu\text{s}$ but shorter $T_2^* = 6.1 \mu\text{s}$. However, we successfully utilize the Carr-Purcell-Meiboom-Gill (CPMG) dynamical-decoupling (DD) pulse sequence to push a DD coherence time T_{2DD} also into 0.1 ms time scale. As shown in Fig. 3a, with the number of π pulses $N_\pi = 1$ (equivalent to one echo pulse), $T_{2DD} = T_{2E} = 22.5 \mu\text{s}$, and with $N_\pi = 4, 16, 64, 256$, $T_{2DD} = 40.6, 56.1, 71.1, 88.0 \mu\text{s}$. While systematic analysis of the qubit noise spectra and their correlation with solid Ne quality is underway, the above observations evidence that solid Ne can indeed serve as a superior host material for electron qubits.

Readout and gate fidelities

We then determine the readout and gate fidelities in

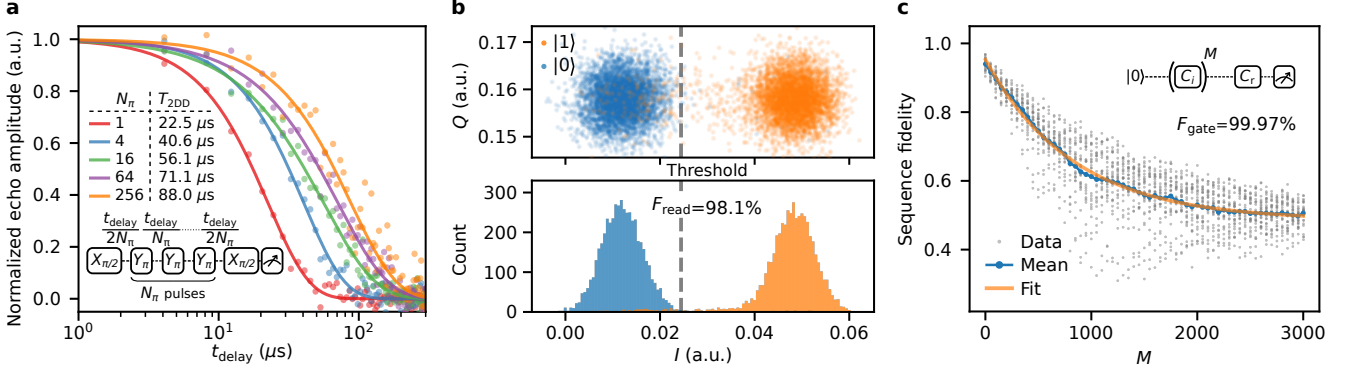


Fig. 3 | Dynamical decoupling, single-shot readout fidelity, and single-qubit gate fidelity of an electron-on-solid-neon (eNe) charge qubit. **a**, Normalized echo amplitude versus the total delay time t_{delay} for different number N_π of CPMG dynamical-decoupling pulses. With $N_\pi = 256$, $T_{2\text{DD}} = 88.0 \mu\text{s}$ is one order of magnitude longer than the $T_2^* = 6.1 \mu\text{s}$ for this qubit. **b**, Single-shot distribution of 5000 readout values for the qubit states prepared in $|0\rangle$ or $|1\rangle$ using $5 \mu\text{s}$ readout pulses and without using a quantum-limited amplifier. The color dots represent the demodulated in-phase (I) and quadrature (Q) readout signals of the qubit. The largest separation of the two readout clouds is aligned along the I axis through demodulation. The overlapped area yields a single-shot readout fidelity $F_{\text{read}} = 98.1\%$. **c**, Single-qubit gate fidelity measurement using the Clifford-based randomized benchmarking technique. The Clifford sequence applied to the qubit in the ground state contains M Clifford gates C_i that are randomly chosen from the Clifford group, followed by a recovery Clifford gate C_r , which (ideally) sets the qubit back to the ground state. The mean sequence fidelity at every Clifford depth M are averaged over 30 random sequences (gray dots) with 1000 times of measurement for each sequence. A power-law fit (orange line) of the mean sequence fidelity (blue dotted line) versus M yields an average single-qubit gate fidelity $F_{\text{gate}} = 99.97\%$.

the eNe qubit system. The qubit with a long $T_1 = 82.8 \mu\text{s}$ on the sweet spot allows us to use long ($\gtrsim 5 \mu\text{s}$) readout pulses without relying on a quantum-limited amplifier. Figure 3b shows the distribution of single-shot readout values for the qubit states prepared in $|0\rangle$ or $|1\rangle$. It yields a single-shot readout fidelity $F_{\text{read}} = 98.1\%$ ⁴⁵. This is higher than the reported 94.7% of superconducting transmon qubits with a similar amplification chain^{27,28}.

The single-qubit gate fidelity for the same qubit is found by Clifford-based randomized benchmarking technique^{29,46}. In this protocol, a Clifford gate sequence with an increasing number M of random Clifford gates and one recovery gate is applied to the qubit in the ground state. Each gate pulse has a Gaussian shape truncated at 2.5 standard deviation ($\sigma = 8 \text{ ns}$) on each side. A separation time of 20 ns is inserted between every two nearest pulses. The decay of the mean sequence fidelity versus M gives an estimate of the average single-qubit gate fidelity $F_{\text{gate}} = 99.97\%$, as shown in Fig. 3c, that is well over the threshold for quantum error correction with surface codes³⁰.

Two qubits strong coupling

Beyond the accomplished single-qubit operations, we are able to load two qubits onto the same trap and spectroscopically bring them on and off resonance with the resonator and show strong coupling for each of them. This is the first step to achieve two-qubit entangling gates in a cQED architecture.

We tune the two qubits by concurrently varying two independent parameters: the offset resonator voltage ΔV_r and the resonator-guard voltage ΔV_{rg} . We call

the qubit with larger coupling strength as qubit-1 and the other as qubit-2. Their frequencies f_{q1} and f_{q2} have different voltage dependence. The upper row of Fig. 4 displays the experimental measurements of the normalized transmission amplitude $(A/A_0)^2$ of the resonator at the bare resonance frequency, with variable ΔV_r and ΔV_{rg} . With obtained qubits properties from the experiments, theoretical calculations based on the Tavis-Cummings model⁴⁷ and the input-output formalism⁴⁸ (see Methods) show excellent agreement with the experiments, as plotted in the lower row.

The two dark lines in Fig. 4a indicate the qubit-resonator on-resonance condition, $f_{q1} = f_r$ and $f_{q2} = f_r$, respectively. The parameter space $(\Delta V_{\text{rg}}, \Delta V_r)$ is divided by the two dark lines into four regions: $(f_{q1}, f_{q2}) > f_r$, $(f_{q1}, f_{q2}) < f_r$, $f_{q1} > f_r > f_{q2}$, and $f_{q1} < f_r < f_{q2}$. A notable feature is that $(A/A_0)^2$ is smaller in the $(f_{q1}, f_{q2}) > f_r$ and $(f_{q1}, f_{q2}) < f_r$ two regions, compared with the other regions. In these two regions, both qubits push the resonator frequency in the same direction due to the strong qubits-resonator coupling, resulting a larger resonator frequency shift and thus a smaller transmission amplitude, as verified by the theoretical calculation.

Figure 4b shows the system spectrum when the two qubits are individually brought onto resonance with the resonator by a tunable ΔV_{rg} and a fixed $\Delta V_r = 5.2 \text{ mV}$, as indicated by the magenta arrows in Fig. 4a. We can retrieve the coupling strength $g_1/2\pi = 3.6 \text{ MHz}$, $g_2/2\pi = 1.8 \text{ MHz}$, and the qubit linewidth $\gamma_1/2\pi = 1.5 \text{ MHz}$, $\gamma_2/2\pi = 1.6 \text{ MHz}$ from the individual vacuum Rabi splitting. Figure 4c shows the system spectrum

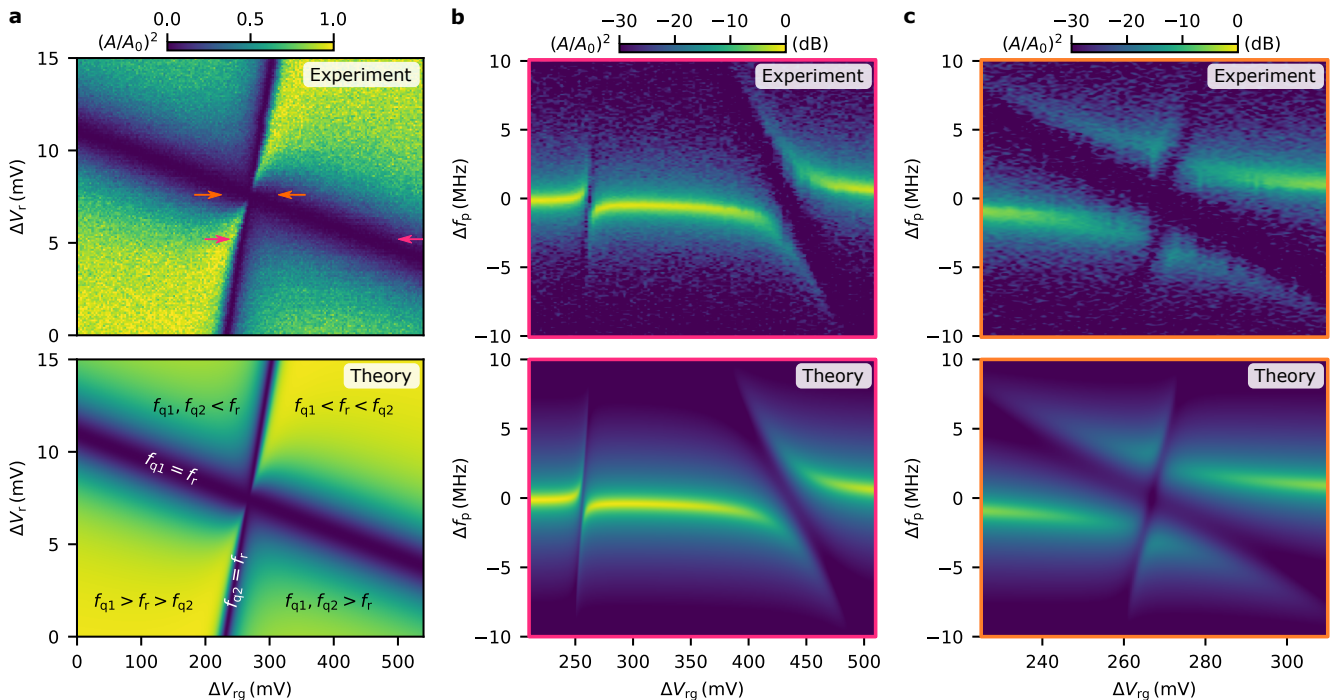


Fig. 4 | Spectroscopic characterization of two electron-on-solid-neon (eNe) charge qubits coupled to a resonator. Upper row shows the experimental observation and lower row shows the theoretical calculation. The qubit with a larger or smaller coupling strength is labeled as qubit-1 or qubit-2, respectively. **a**, Spectral tuning of two qubits. The microwave transmission amplitude $(A/A_0)^2$ through the resonator probed at the bare resonator frequency $f_p = f_r$ is plotted against the offset resonator voltage ΔV_r and resonator-guard voltage ΔV_{rg} . The parameter space $(\Delta V_{rg}, \Delta V_r)$ is divided into four regions by the two dark lines that correspond to each qubit being individually on resonance with the resonator. The relations between f_{q1} , f_{q2} and f_r in the four regions and along the two lines are labeled in the lower panel. At the crossing of two dark lines marked by the orange arrows, the two qubits are simultaneously on resonance with the resonator. **b**, $(A/A_0)^2$ versus $\Delta f_p = f_p - f_r$ and ΔV_{rg} along the line indicated by the pink arrows in **a**, where the two qubits can be individually on resonance with the resonator. **c**, $(A/A_0)^2$ versus Δf_p and ΔV_{rg} along the line indicated by the orange arrows in **a**, where the two qubits can be simultaneously on resonance with the resonator.

when the two qubits are simultaneously brought onto resonance with the resonator by a tunable ΔV_{rg} and another fixed $\Delta V_r = 7.4$ mV, as indicated by the orange arrows in Fig. 4a. At $\Delta V_{rg} = 267$ mV, the resonator is simultaneously hybridized with both qubits.

Discussion and outlook

While our measured coherence time for an eNe qubit has approached 0.1ms, we believe that it can be further improved by optimizing our device design, drive scheme, and solid-Ne growth procedure. Solely from the material perspective, we do not foresee a practical limit on the charge-qubit coherence time in this system, though theoretical calculation can be done to find out the ultimate decoherence due to thermal phonons or quantum zero-point motion of Ne atoms^{49–52}.

The anharmonicity α , defined as the frequency difference between the $|g\rangle \rightarrow |e\rangle$ and $|e\rangle \rightarrow |f\rangle$ transitions with $|f\rangle$ being the second excited state, is a critical parameter for the gate time. A larger α ensures a shorter gate time³⁹. For our qubit, α is estimated to be greater than 1 GHz, based on the large detuning range and strong pumping power that we have explored. We were not

able to observe a $|g\rangle \rightarrow |f\rangle$ two-photon transition or a $|e\rangle \rightarrow |f\rangle$ one-photon transition after preparing the qubit on $|e\rangle$. We shall note that even for an infinite α , which corresponds to an ideal two-level system, the theoretical dispersive shift would be $\chi = g^2/\Delta = -0.152$ MHz, which is close to our measured -0.13 MHz. This is another evidence that our α is very larger, $\alpha \gg |\Delta|$.

While we have managed to simultaneously couple two electron qubits to the same resonator, to realize two-qubit gates in real time in the cQED architecture, we need to push on from the strong resonant regime into the strong dispersive regime. This requires larger g/γ and g/κ ⁵³. In light of the observed $\gamma/2\pi \lesssim 0.02$ MHz at the charge sweet spot, g/γ already satisfies the strong dispersive requirement. To keep fast operations, the resonator linewidth κ from the input-output coupling cannot be much smaller than the current $\kappa/2\pi = 0.46$ MHz. Therefore, the coupling strength g should be enhanced by about ten times, optimally. This may be fulfilled by using high kinetic-inductance superconducting materials for the on-chip resonator^{54–56}. Realization of two-qubit gates in the eNe

charge qubit platform will establish a further milestone toward universal quantum computing.

- *These authors contributed equally to this work.
[†]Email: dschus@stanford.edu
[‡]Email: dfjin@nd.edu
- ¹T. D. Ladd, F. Jelezko, R. Laflamme, Y. Nakamura, C. Monroe, and J. L. O’Brien, “Quantum computers,” *Nature* **464**, 45–53 (2010).
 - ²A. Chatterjee, P. Stevenson, S. De Franceschi, A. Morello, N. P. de Leon, and F. Kuemmeth, “Semiconductor qubits in practice,” *Nat. Rev. Phys.* **3**, 157–177 (2021).
 - ³I. Siddiqi, “Engineering high-coherence superconducting qubits,” *Nat. Rev. Mater.* **6**, 875–891 (2021).
 - ⁴P. Stano and D. Loss, “Review of performance metrics of spin qubits in gated semiconducting nanostructures,” *Nat. Rev. Phys.* **4**, 672–688 (2022).
 - ⁵J. T. Muhonen, J. P. Dehollain, A. Laucht, F. E. Hudson, R. Kalra, T. Sekiguchi, K. M. Itoh, D. N. Jamieson, J. C. McCallum, A. S. Dzurak, and A. Morello, “Storing quantum information for 30 seconds in a nanoelectronic device,” *Nat. Nanotechnol.* **9**, 986–991 (2014).
 - ⁶M. Veldhorst, J. C. Hwang, C. H. Yang, A. W. Leenstra, B. De Ronde, J. P. Dehollain, J. T. Muhonen, F. E. Hudson, K. M. Itoh, A. Morello, and A. S. Dzurak, “An addressable quantum dot qubit with fault-tolerant control-fidelity,” *Nat. Nanotechnol.* **9**, 981–985 (2014).
 - ⁷J. Yoneda, K. Takeda, T. Otsuka, T. Nakajima, M. R. Delbecq, G. Allison, T. Honda, T. Kodera, S. Oda, Y. Hoshi, N. Usami, K. M. Itoh, and S. Tarucha, “A quantum-dot spin qubit with coherence limited by charge noise and fidelity higher than 99.9%,” *Nat. Nanotechnol.* **13**, 102–106 (2018).
 - ⁸L. B. Nguyen, Y. H. Lin, A. Somoroff, R. Mencia, N. Grabon, and V. E. Manucharyan, “High-coherence fluxonium qubit,” *Phys. Rev. X* **9**, 041041 (2019).
 - ⁹A. Somoroff, Q. Ficheux, R. A. Mencia, H. Xiong, R. V. Kuzmin, and V. E. Manucharyan, “Millisecond coherence in a superconducting qubit,” arXiv:2103.08578 (2021).
 - ¹⁰A. P. Place, L. V. Rodgers, P. Mundada, B. M. Smitham, M. Fitzpatrick, Z. Leng, A. Premkumar, J. Bryon, A. Vrajitoarea, S. Sussman, G. Cheng, T. Madhavan, H. K. Babla, X. H. Le, Y. Gang, B. Jäck, A. Gyenis, N. Yao, R. J. Cava, N. P. de Leon, and A. A. Houck, “New material platform for superconducting transmon qubits with coherence times exceeding 0.3 milliseconds,” *Nat. Commun.* **12**, 1779 (2021).
 - ¹¹C. Wang, X. Li, H. Xu, Z. Li, J. Wang, Z. Yang, Z. Mi, X. Liang, T. Su, C. Yang, G. Wang, W. Wang, Y. Li, M. Chen, C. Li, K. Linghu, J. Han, Y. Zhang, Y. Feng, Y. Song, T. Ma, J. Zhang, R. Wang, P. Zhao, W. Liu, G. Xue, Y. Jin, and H. Yu, “Towards practical quantum computers: transmon qubit with a lifetime approaching 0.5 milliseconds,” *npj Quantum Inf.* **8**, 3 (2022).
 - ¹²A. J. Heinrich, W. D. Oliver, L. M. Vandersypen, A. Ardavan, R. Sessoli, D. Loss, A. B. Jayich, J. Fernandez-Rossier, A. Laucht, and A. Morello, “Quantum-coherent nanoscience,” *Nat. Nanotechnol.* **16**, 1318–1329 (2021).
 - ¹³M. A. Nielsen and I. L. Chuang, *Quantum Computation and Quantum Information* (Cambridge University Press, 2010).
 - ¹⁴D. Kim, D. R. Ward, C. B. Simmons, J. K. Gamble, R. Blume-Kohout, E. Nielsen, D. E. Savage, M. G. Lagally, M. Friesen, S. N. Coppersmith, and M. A. Eriksson, “Microwave-driven coherent operation of a semiconductor quantum dot charge qubit,” *Nat. Nanotechnol.* **10**, 243–247 (2015).
 - ¹⁵K. Takeda, J. Kamioka, T. Otsuka, J. Yoneda, T. Nakajima, M. R. Delbecq, S. Amaha, G. Allison, T. Kodera, S. Oda, and S. Tarucha, “A fault-tolerant addressable spin qubit in a natural silicon quantum dot,” *Sci. Adv.* **2**, e1600694 (2016).
 - ¹⁶A. Osman, J. Simon, A. Bengtsson, S. Kosen, P. Krantz, D. P. Lozano, M. Scigliuzzo, P. Delsing, J. Bylander, and A. Fadavi Roudsari, “Simplified Josephson-junction fabrication process for reproducibly high-performance superconducting qubits,” *Appl. Phys. Lett.* **118**, 064002 (2021).
 - ¹⁷Y. A. Pashkin, O. Astafiev, T. Yamamoto, Y. Nakamura, and J. S. Tsai, “Josephson charge qubits: A brief review,” *Quantum Inf. Process.* **8**, 55–80 (2009).
 - ¹⁸N. Samkharadze, A. Bruno, P. Scarlino, G. Zheng, D. DiVincenzo, L. DiCarlo, and L. Vandersypen, “High-kinetic-inductance superconducting nanowire resonators for circuit qed in a magnetic field,” *Phys. Rev. Appl.* **5**, 044004 (2016).
 - ¹⁹J. Kroll, F. Borsoi, K. Van Der Enden, W. Uilhoorn, D. De Jong, M. Quintero-Pérez, D. Van Woerkom, A. Bruno, S. Plissard, D. Car, E. Bakkers, M. Cassidy, and L. Kouwenhoven, “Magnetic-field-resilient superconducting coplanar-waveguide resonators for hybrid circuit quantum electrodynamics experiments,” *Phys. Rev. Appl.* **11**, 064053 (2019).
 - ²⁰A. Blais, A. L. Grimsmo, and A. Wallraff, “Circuit quantum electrodynamics,” *Rev. Mod. Phys.* **93**, 025005 (2021).
 - ²¹B. D’Anjou and G. Burkard, “Optimal dispersive readout of a spin qubit with a microwave resonator,” *Phys. Rev. B* **100**, 245427 (2019).
 - ²²X. Hu, Y. Liu, and F. Nori, “Strong coupling of a spin qubit to a superconducting stripline cavity,” *Phys. Rev. B* **86**, 035314 (2012).
 - ²³X. Zhou, G. Koolstra, X. Zhang, G. Yang, X. Han, B. Dizdar, X. Li, D. Ralu, W. Guo, K. W. Murch, D. I. Schuster, and D. Jin, “Single electrons on solid neon as a solid-state qubit platform,” *Nature* **605**, 46–50 (2022).
 - ²⁴V. Zavyalov, I. Smolyaninov, E. Zotova, A. Borodin, and S. Bogomolov, “Electron states above the surfaces of solid cryodielectrics for quantum-computing,” *J. Low Temp. Phys.* **138**, 415–420 (2005).
 - ²⁵C. D. Wilen, S. Abdullah, N. A. Kurinsky, C. Stanford, L. Cardani, G. D’Imperio, C. Tomei, L. Faoro, L. B. Ioffe, C. H. Liu, A. Opremcak, B. G. Christensen, J. L. DuBois, and R. McDermott, “Correlated charge noise and relaxation errors in superconducting qubits,” *Nature* **594**, 369–373 (2021).
 - ²⁶P. Leiderer, K. Kono, and D. Rees, in *Proc. 11th International Conference on Cryocrystals and Quantum Crystals*, edited by S. Vasiliev (2016) pp. 67–67.
 - ²⁷F. Mallet, F. R. Ong, A. Palacios-Laloy, F. Nguyen, P. Bertet, D. Vion, and D. Esteve, “Single-shot qubit readout in circuit quantum electrodynamics,” *Nat. Phys.* **5**, 791–795 (2009).
 - ²⁸L. Stefanazzi, K. Treptow, N. Wilcer, C. Stoughton, C. Bradford, S. Uemura, S. Zorzetti, S. Montella, G. Cancelo, S. Sussman, A. Houck, S. Saxena, H. Arnaldi, A. Agrawal, H. Zhang, C. Ding, and D. I. Schuster, “The QICK (Quantum Instrumentation Control Kit): Readout and control for qubits and detectors,” *Rev. Sci. Instrum.* **93**, 044709 (2022).
 - ²⁹E. Knill, D. Leibfried, R. Reichle, J. Britton, R. B. Blakestad, J. D. Jost, C. Langer, R. Ozeri, S. Seidelin, and D. J. Wineland, “Randomized benchmarking of quantum gates,” *Phys. Rev. A* **77**, 012307 (2008).
 - ³⁰A. G. Fowler, M. Mariantoni, J. M. Martinis, and A. N. Cleland, “Surface codes: Towards practical large-scale quantum computation,” *Phys. Rev. A* **86**, 032324 (2012).
 - ³¹D. P. DiVincenzo, D. Bacon, J. Kempe, G. Burkard, and K. B. Whaley, “Universal quantum computation with the exchange interaction,” *Nature* **408**, 339–342 (2000).
 - ³²G. Koolstra, G. Yang, and D. I. Schuster, “Coupling a single electron on superfluid helium to a superconducting resonator,” *Nat. Commun.* **10**, 5323 (2019).
 - ³³R. T. Jacobsen, S. G. Penoncello, and E. W. Lemmon, “Thermodynamic properties of cryogenic fluids,” in *Thermodynamic Properties of Cryogenic Fluids* (Springer, 1997) pp. 31–287.
 - ³⁴F. Mugele, U. Albrecht, P. Leiderer, and K. Kono, “Possible correlation effects of surface state electrons on a solid hydrogen film,” *J. Low Temp. Phys.* **89**, 743–746 (1992).
 - ³⁵D. I. Schuster, A. Fragner, M. I. Dykman, S. A. Lyon, and R. J. Schoelkopf, “Proposal for manipulating and detecting spin and orbital states of trapped electrons on helium using cavity

- quantum electrodynamics,” *Phys. Rev. Lett.* **105**, 040503 (2010).
- ³⁶E. Kawakami, A. Elarabi, and D. Konstantinov, “Image-charge detection of the rydberg states of surface electrons on liquid helium,” *Phys. Rev. Lett.* **123**, 086801 (2019).
- ³⁷D. I. Schuster, A. Wallraff, A. Blais, L. Frunzio, R. S. Huang, J. Majer, S. M. Girvin, and R. J. Schoelkopf, “ac Stark shift and dephasing of a superconducting qubit strongly coupled to a cavity field,” *Phys. Rev. Lett.* **94**, 123602 (2005).
- ³⁸D. Vion, A. Aassime, A. Cottet, P. Joyez, H. Pothier, C. Urbina, D. Esteve, and M. H. Devoret, “Manipulating the quantum state of an electrical circuit,” *Science* **296**, 886–889 (2002).
- ³⁹P. Krantz, M. Kjaergaard, F. Yan, T. P. Orlando, S. Gustavsson, and W. D. Oliver, “A quantum engineer’s guide to superconducting qubits,” *Appl. Phys. Rev.* **6**, 021318 (2019).
- ⁴⁰L. Allen and J. H. Eberly, *Optical Resonance and Two-Level Atoms* (Dover, New York, 1987).
- ⁴¹R. Bianchetti, S. Filipp, M. Baur, J. M. Fink, M. Göppl, P. J. Leek, L. Steffen, A. Blais, and A. Wallraff, “Dynamics of dispersive single-qubit readout in circuit quantum electrodynamics,” *Phys. Rev. A* **80**, 043840 (2009).
- ⁴²E. M. Purcell, “Spontaneous emission probabilities at radio frequencies,” *Phys. Rev.* **69**, 681 (1946).
- ⁴³E. A. Sete, J. M. Gambetta, and A. N. Korotkov, “Purcell effect with microwave drive: Suppression of qubit relaxation rate,” *Phys. Rev. B* **89**, 104516 (2014).
- ⁴⁴J. Verjauw, R. Acharya, J. Van Damme, T. Ivanov, D. P. Lozano, F. Mohiyaddin, D. Wan, J. Jussot, A. Vadiraj, M. Mongillo, M. Heyns, I. Radu, B. Govoreanu, and A. Potočnik, “Path toward manufacturable superconducting qubits with relaxation times exceeding 0.1 ms,” arXiv:2202.10303 (2022).
- ⁴⁵J. Gambetta, W. A. Braff, A. Wallraff, S. M. Girvin, and R. J. Schoelkopf, “Protocols for optimal readout of qubits using a continuous quantum nondemolition measurement,” *Phys. Rev. A* **76**, 012325 (2007).
- ⁴⁶R. Barends, J. Kelly, A. Megrant, A. Veitia, D. Sank, E. Jeffrey, T. C. White, J. Mutus, A. G. Fowler, B. Campbell, Y. Chen, Z. Chen, B. Chiaro, A. Dunsworth, C. Neill, P. O’Malley, P. Roushan, A. Vainsencher, J. Wenner, A. N. Korotkov, A. N. Cleland, and J. M. Martinis, “Superconducting quantum circuits at the surface code threshold for fault tolerance,” *Nature* **508**, 500–503 (2014).
- ⁴⁷M. Tavis and F. Cummings, “Exact solution for an n-molecule-radiation-field hamiltonian,” *Phys. Rev.* **170**, 379–384 (1968).
- ⁴⁸D. F. Walls and G. J. Milburn, *Quantum Optics* (Springer Science & Business Media, 2007).
- ⁴⁹M. I. Dykman, P. M. Platzman, and P. Seddighrad, “Qubits with electrons on liquid helium,” *Phys. Rev. B* **67**, 155402 (2003).
- ⁵⁰Q. Chen, I. Martin, L. Jiang, and D. Jin, “Electron spin coherence on a solid neon surface,” *Quantum Sci. and Technol.* **7**, 045016 (2022).
- ⁵¹G. L. Pollack, “The solid state of rare gases,” *Rev. Mod. Phys.* **36**, 748 (1964).
- ⁵²M. L. Klein and J. A. Venables, *Rare Gas Solids*, Vol. I (Academic, New York, 1976).
- ⁵³D. I. Schuster, *Circuit Quantum Electrodynamics*, Ph.D. thesis, Yale University (2007).
- ⁵⁴A. Shearow, G. Koolstra, S. J. Whiteley, N. Earnest, P. S. Barry, F. J. Heremans, D. D. Awschalom, E. Shirokoff, and D. I. Schuster, “Atomic layer deposition of titanium nitride for quantum circuits,” *Appl. Phys. Lett.* **113**, 212601 (2018).
- ⁵⁵M. Xu, X. Han, W. Fu, C.-L. Zou, and H. X. Tang, “Frequency-tunable high-q superconducting resonators via wireless control of nonlinear kinetic inductance,” *Appl. Phys. Lett.* **114**, 192601 (2019).
- ⁵⁶X. Han, C.-L. Zou, W. Fu, M. Xu, Y. Xu, and H. X. Tang, “Superconducting cavity electromechanics: The realization of an acoustic frequency comb at microwave frequencies,” *Phys. Rev. Lett.* **129**, 107701 (2022).

Methods

Qubit-resonator coupled system

Our electron-photon (qubit-resonator) coupled system adopts a cQED architecture. When the qubit and resonator are uncoupled, the qubit has its bare frequency $\omega_q/2\pi = f_q$. In the presence of a finite coupling strength g , the eigenstates of the coupled system are dressed states²⁰. As plotted in Extended Data Fig.1a, in the resonant regime, $f_r = f_q$, the qubit and resonator maximally hybridize, and a vacuum Rabi splitting $2g$ opens up. In the dispersive regime, the detuning $|\Delta = \omega_q - \omega_r| \gg g$, the actual qubit frequency acquires a shift of $(1 + 2\bar{n})\chi$, in which χ is called the dispersive shift, $2\bar{n}\chi$ is called the ac Stark shift, and \bar{n} is the average intra-resonator photon number. In this regime, the actual resonator frequency acquires a $+\chi$ or $-\chi$ shift, when the qubit is kept in the excited or ground state, respectively.

ac Stark effect

We use the two-tone qubit spectroscopy to demonstrate the ac Stark effect and calibrate the average intra-resonator photon number \bar{n} . Keeping $V_{rg} = V_{ss}$ on the sweet spot and the drive power P_d low, we scan both the drive frequency f_d and the probe power P_p . In this scenario, \bar{n} increases with the increasing P_p and the qubit frequency f_q shifts under the ac Stark effect³⁷. Extended Data Fig.1b gives a series of curves of ϕ versus f_d with step-increased P_p . The detected f_q is red-shifted by $\delta f_{ac} \approx -6$ MHz when P_p (from the vector network analyzer) is increased from -20 dBm to 0 dBm. This shift is related to the average intra-resonator photon number \bar{n} by $\delta f_{ac} = \chi\bar{n}/\pi$ ³⁷. Through this measurement, and the measurement of χ (see below), we know that a probe power $P_p < -13$ dBm ≈ 0.05 mW (about -135 dBm reaching the sample) corresponds to $\bar{n} < 1$.

Dispersive readout

The qubit readout follows the standard dispersive readout scheme, where the qubit states are inferred from measuring the phase or amplitude shift of the transmission $S_{21}(f_p)$ through the resonator. The readout is performed with $\bar{n} < 1$. As shown in Extended Data Fig.1c, the resonator frequency is dispersively shifted to $f_r + \chi/2\pi$ or $f_r - \chi/2\pi$, when the qubit is in the excited state $|1\rangle$ or ground state $|0\rangle$. Here on the sweet spot, we have $\chi/2\pi = -0.13$ MHz. The dispersive readout has the highest contrast by fixing the probe frequency f_p at the bare resonance frequency f_r indicated by the gray line, where the phase separation between $|0\rangle$ and $|1\rangle$ is maximal.

Theoretical modeling of two qubits coupling

The behavior of a system consisting of two qubits interacting with a single-mode resonator can be theoretically described by the Tavis-Cummings (TC) Hamiltonian in the rotating-wave approximation⁴⁷,

$$\hat{H} = \hbar\omega_r\hat{a}^\dagger\hat{a} + \sum_j \left[\hbar\omega_j\hat{\sigma}_j^\dagger\hat{\sigma}_j + \hbar g_j \left(\hat{a}^\dagger\hat{\sigma}_j + \hat{a}\hat{\sigma}_j^\dagger \right) \right], \quad (1)$$

where $j = 1, 2$ and $\omega_r = 2\pi f_r$ is the resonator frequency, \hat{a}^\dagger and \hat{a} are the creation and annihilation operators of

microwave photons, $\omega_j = 2\pi f_j$ is the qubit j frequency, and g_j is the coupling strength between the qubit j and the resonator, $\hat{\sigma}_j = \hat{\sigma}_j^x - i\hat{\sigma}_j^y$ and $\hat{\sigma}_j^\dagger = \hat{\sigma}_j^x + i\hat{\sigma}_j^y$ are the ladder operators acting on the qubit j .

Using the quantum master equation and input-output theory⁴⁸, assisted with the known quantities directly measured from experiments, such as the resonator linewidth κ , we can theoretically calculate all the normalized transmission amplitude $(A/A_0)^2$ through the resonator versus the qubit frequency f_j and probe frequency f_p . The only phenomenological modeling necessary is the relations between the qubit frequencies and applied voltages, which we assume to be linear functions.

Data availability

The raw data that support the findings of this study are available from the corresponding author upon reasonable request.

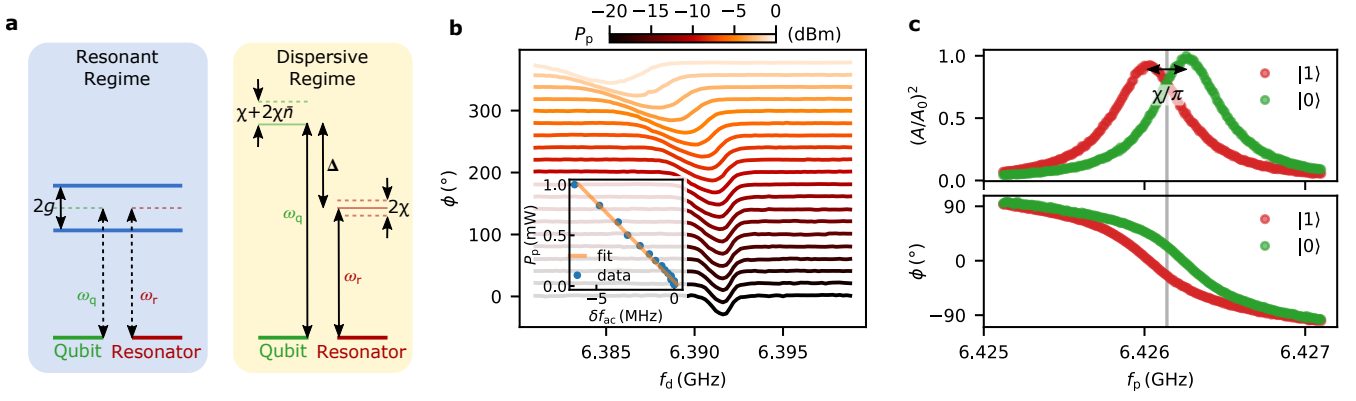
Code availability

The codes used to perform the experiments and to analyze the data in this work are available from the corresponding author upon reasonable request.

ACKNOWLEDGMENTS

Work performed at the Center for Nanoscale Materials, a U.S. Department of Energy Office of Science User Facility, was supported by the U.S. DOE, Office of Basic Energy Sciences, under Contract No. DE-AC02-06CH11357. D.J., X.H., X.L., and Q.C. acknowledge support from Argonne National Laboratory Directed Research and Development (LDRD). D.J. and X.Zhou acknowledge support from the Julian Schwinger Foundation for Physics Research. This work was partially supported by the University of Chicago Materials Research Science and Engineering Center, which is funded by the National Science Foundation under award number DMR-2011854. This work made use of the Pritzker Nanofabrication Facility of the Institute for Molecular Engineering at the University of Chicago, which receives support from SHyNE, a node of the National Science Foundation National Nanotechnology Coordinated Infrastructure (NSF NNCI-1542205). D.I.S. and B.D. acknowledge support from the National Science Foundation DMR grant DMR-1906003. D.I.S. and C.S.W. acknowledge support from the U.S. Department of Energy, Office of Science, National Quantum Information Science Research Centers. G.Y. acknowledges supports from the National Science Foundation under Cooperative Agreement PHY-2019786 (the NSF AI Institute for Artificial Intelligence and Fundamental Interactions). D.J. thanks Anthony J. Leggett for inspiring discussions. The qubit manipulation and measurement in this work utilized the highly efficient and effective OPX+, Octave,

and QDAC-II made by Quantum Machines and QDevil.



Extended Data Fig. 1 | Qubit-resonator coupled spectrum, ac Stark shift, and dispersive shift. **a**, Schematic of the qubit-resonator coupled spectrum. $\omega_q = 2\pi f_q$ is the bare qubit frequency, $\omega_r = 2\pi f_r$ is the bare resonator frequency, and g is the coupling strength. In the resonant regime, $f_r = f_q$, the qubit and resonator hybridize and a vacuum Rabi splitting $2g$ opens up. In the dispersive regime, the detuning $|\Delta = \omega_q - \omega_r| \gg g$, the actual qubit frequency exhibits the dispersive shift χ and the ac Stark shift $2\chi\bar{n}$, in which \bar{n} is the average intra-resonator photon number, whereas the actual resonator frequency exhibits a $+\chi$ or $-\chi$ shift, when the qubit is kept in the excited or ground state, respectively. **b**, Observation of the ac Stark shift. The transmission phase ϕ at $f_p = f_r$ is plotted versus f_d and probe power P_p , when the qubit is on the sweet spot in Fig. 1d. With increasing P_p , the qubit frequency is red-shifted because of the ac Stark effect. In the inset, the frequency shift δf_{ac} shows a linear dependence on P_p (equivalent to the average intra-resonator photon number \bar{n}). **c**, Measurement of the state-dependent dispersive shift. Normalized transmission amplitude $(A/A_0)^2$ (top) and phase ϕ (bottom) are plotted versus the probe frequency f_p when the qubit is in the ground state $|0\rangle$ or excited state $|1\rangle$. The grey line corresponds to $f_p = f_r$, where f_r is the bare resonator frequency. The measured dispersive shift is $\chi/2\pi = -0.13$ MHz.